Communications in Computational Chemistry
Commun. Comput. Chem., Vol. 1, No. 1, 71–80
doi: 10.4208/cicc.2025.74.01
Regular Article

First Principles Calculations on Atomistic Mechanisms of Surface/Interface-Induced Properties and Database Construction

Zehai Zhang[1,2,†], Lei Tao[2,†] and Shixuan Du[1,2,3,*]

[1]*Beijing National Laboratory for Condensed Matter Physics, Institute of Physics, Chinese Academy of Sciences, Beijing 100190, P. R. China;*

[2]*School of Physics, University of Chinese Academy of Sciences, Beijing 100049, P. R. China;*

[3]*Songshan Lake Materials Laboratory, Dongguan 523808, P. R. China.*

[*] Corresponding authors: ShiXuan Du, sxdu@iphy.ac.cn

Received on 15 March 2025; Accepted on 11 April 2025

Abstract: Surfaces and interfaces play a critical role in exploring novel chemical and physical properties because the interactions between surface and adsorbents, as well as interfacial interactions, can be finely tuned by the interface configurations at the atomic level across a wide range, from strong covalent and ionic bonds to weak hydrogen bonds and van der Waals interactions. These interactions enable precise control over molecular adsorption, self-assembly, and activation, facilitating the design of nanostructures and modulation of novel properties. Recent developments in computational technologies, including high-throughput screening and machine learning, have significantly accelerated the discovery of functional materials. This review highlights theoretical progress in manipulating the physical and chemical properties of organic molecules at surfaces and interfaces, with a focus on controlling molecular configuration and magnetism, selective activation, on-surface synthesis, and interfacial engineering of 2D materials. Our goal is to understand the key factors influencing the physical and chemical properties at surfaces and interfaces, with a particular focus on theoretical insights and computational approaches.

Key words: surface chemistry, interface chemistry, computational simulation, 2D materials, molecular adsorption.

1. Introduction

Surfaces and interfaces serve as critical platforms for exploring novel chemical and physical properties due to their ability to provide unique and tunable interactions across a wide energy range [1,2]. For instance, the strength of covalent bonds typically ranges from 1 to 10 eV, while ionic bonds have strengths between 2 and 4 eV. In contrast, hydrogen bonds and van der Waals (vdWs) interactions are much weaker, with energies ranging from 0.01 to 0.4 eV for hydrogen bonds and 0.001 to 0.01 eV for vdWs interactions. Furthermore, the symmetry of surface structures, along with variations in potential energy surfaces at different sites, enables the adsorption [3], assembly [4], and activation processes [5] on surfaces to be finely tuned. For example, exchange interactions in magnetic materials, which typically occur at the meV level, are comparable in magnitude to vdWs interactions. It enables the modulation of magnetic properties through weak adsorption at surfaces or interfaces [6]. Moreover, thermal excitation of molecules on surfaces at elevated temperatures involves energies between 0.1 and 1 eV, which can drive the breaking or reforming of chemical bonds. This provides a pathway for atomic-level design and engineering of novel nanostructures [7]. The rapid development of two-dimensional (2D) materials over the past decade has not only enabled the modification using thermal [5], optical [8-10], magnetic [11] and electric field [12] approaches, but also allows for tuning through mechanical methods such as stretching and folding [13]. These advantages result in significant increases in the potential applications of nanomaterial-based devices [14], including nanorecording [15-19], asymmetric

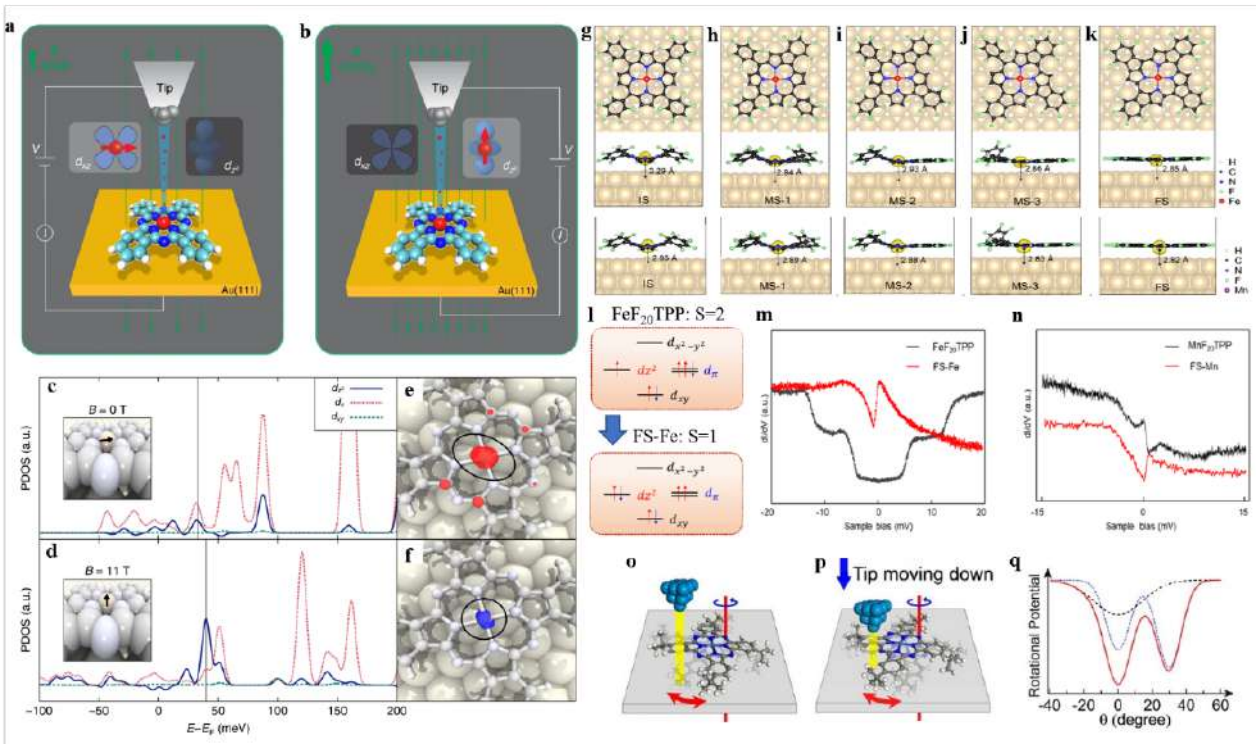

Figure 1. Magnetic, intramolecular cyclization and mechanical regulation of M-Pc molecules. **a**, **b** Schematics of the electron transport process through an FePc molecule adsorbed on a Au(111) surface at different magnetic fields. **c**, **d** Calculated lm-decomposed partial density of states (PDOS) of the Fe atom (d_π represents d_{xz} or d_{yz}). **e**, **f** Band-decomposed charge density plots for the molecular orbitals close to E_F, showing the spatial distribution of the Kondo resonance. **g-k** DFT calculated the adsorption configurations and spin density distributions of IS, MS1, MS2, MS3 and FS on Au(111). **l**, Schematic representations of the transition from the S = 2 electronic state of $FeF_{20}TPP$ to the S = 1 electronic state of the final state (FS). **m** The differential conductance dI/dV spectra acquired upon the center of the $FeF_{20}TPP$ and FS-Fe molecules. The dip-like feature around zero bias voltage and symmetric steps represents Kondo resonance (red curve) and IETS (black curve). **n** The differential conductance dI/dV spectra acquired upon the center of the $MnF_{20}TPP$ and FS-Mn molecules. The conductance dip (or peak) near zero energy represents Kondo resonance (red line and black line) (V_s=-20 mV, I_t=300 pA, lock-in modulation: V_{rms}=0.5 mV). **o** Sketch of the dominant adsorption configuration of $(t\text{-}Bu)_4$-NiPc on Au(111) when the tip is far away. **p** Sketch of adsorption configuration of $(t\text{-}Bu)_4$-NiPc after the tip approaches the sample surface. **q** Schematic representation of the rotational potential energy around two configurations consisting of the native potential well without tip molecule interaction (blue dotted line); the tip-induced potential well (black dashed line); the potential landscape with added contributions of the native and tip-induced potentials (red solid line). $V_{Sample} = -1$ V and the feedback loop is open.

catalysis [20], giant magnetoresistive devices [6], molecular machines [21-24], and spintronics [12,25,26].

In recent years, the development of computational technologies has enabled data-driven paradigms in materials science, including high-throughput screening and machine learning, accelerating the design of functional materials. Within these paradigms, high-quality databases are recognized as the foundations, because one can both efficiently identify high-performance functional materials and use those databases as extensive data resources for training machine learning model.

In this review, we present the recent progress from a theoretical perspective on manipulating physical and chemical properties at surfaces and interfaces, and constructing databases based on the deep insights into the structure-property relations. First, we discuss various methods for controlling the molecular configuration and magnetism of organic molecules utilizing magnetic fields, electric fields, and intramolecular cyclization. Next, we focus on the selective activation of organic molecules and highlight strategies for the bottom-up synthesis of graphene nanoribbons through surface activation. Finally, we explore interfacial engineering of 2D materials, from weak van der Waals stacking to strong interlayer interactions via covalent and ionic bonds.

2. Surface-induced physicochemical properties

2.1. Novel properties of single molecule on surface

Metal-phthalocyanines (M-Pc) and metal-porphyrins (M-PP) are versatile functional molecules widely used in catalysis and organic electronics due to their unique optical and electrochemical properties [27,28]. Their ability to form stable complexes with metal ions and exhibit strong light absorption makes them ideal for applications in solar cells, sensors, and molecular devices [29,30]. For example, Yang *et al.* used scanning tunneling microscopy (STM) to investigate the transport of a single FePc molecule, demonstrating how an external magnetic field can control the spin states and conductance [6]. Notably, the Fe ion in FePc is located at bridge site with a magnetic moment of 2μB. At weak fields (as shown in **Figure 1a**), the spin is in-plane, and electrons flow via the d_{xz}/d_{yz} orbitals. At stronger fields (as shown in **Figure 1b**), the spin aligns with the field, and tunneling occurs through the d_{z2} orbital. **Figure 1(c-f)** show that increasing magnetic field intensity alters the transmission path from

d_{xz}/d_{yz} to d_{z2}. The team also achieved control over a giant magnetoresistance effect, with a 93% change in molecular conductance, highlighting the role of spin-orbit coupling and multi-orbital effects in controlling single-electron processes in single-molecule devices.

The spin states of M-Pc molecules play a critical role in molecular electronics and spintronics, where the interaction between the spin electrons in M-Pc and the conduction electrons in the metal substrate can lead to the formation of a Kondo resonance [31]. This Kondo resonance can be modulated by controlling the interaction strength between the metal ion (M) in M-Pc and the metal surface, achieved through a series of intramolecular cyclization reactions of tetrakis(pentafluorophenyl) porphyrin ($FeF_{20}TPP$) molecules [32]. $FeF_{20}TPP$ undergoes a structural transition from a saddle-shaped conformation to a planar configuration [33], resulting in a significant reduction in the Fe-Au distance from 3.29 Å to 2.85 Å. This change indicates a substantial enhancement in the coupling between Fe and Au. During the reaction, the d_{z^2} orbital becomes occupied by 2 electrons, while d_π orbitals have two spin-up electrons, leading to a transition from a high-spin state (S=2) to an intermediate-spin state (S=1). In contrast, for $MnF_{20}TPP$, the Mn-Au distance changes only slightly from 2.95 Å to 2.82 Å, with no significant alteration in the spin state. These findings are corroborated by differential conductance (dI/dV) spectra. As shown in **Figure 1(g-m)**, the initial saddle-shaped $FeF_{20}TPP$ exhibits no Kondo resonance but instead displays two pairs of steps, while the planar product shows a sharp dip near the Fermi level attributed to the Kondo effect. In contrast, both the initial and planar $MnF_{20}TPP$ configurations exhibit pronounced dip features, consistent with the Kondo resonance. Besides, the interaction between FePc and $FeF_{20}TPP$ results in the formation of a 2D Kondo array [34], further demonstrating the tunability of spin-dependent phenomena in these systems.

Furthermore, the molecular configuration can be tuned by electric field, which makes it promising for molecular motors. By introducing a tip-induced electric field, Lu *et al.* modified the effective rotational potential energy of molecular rotors [24]. When an STM tip in tunneling mode was positioned above the outer edge of a rotating molecule, the molecule exhibited rotational hopping, randomly switching between two configurations (shown in **Figure 1o and 1p**). The occupation probability of each configuration is determined by its potential energy, and the transition between configurations at varying tip–molecule distances reveals that the rotational potential energy of the molecular rotor changes with the tip–molecule separation (as shown in **Figure 1q**).

2.2. Selective activation and on-surface synthesis

Selective activation of organic molecules is crucial in chemical synthesis to achieve high selectivity for a single product among multiple isomers. One key approach is controlling site selectivity, which involves differentiating the reactivity among identical functional groups within a molecule. At low coverage, site-selective adsorption is driven by molecule-surface interactions, leading to symmetry-breaking of the reactant and enabling selective activation at elevated temperatures. As coverage increases, intermolecular interactions introduce steric hindrance, further enhancing site selectivity [32]. Additionally, the self-assembly that forms at high coverage acts as a well-ordered template, which can be utilized in on-surface synthesis to fabricate low-dimensional supramolecular networks [35,36].

In this section, we first introduce theoretical strategies for distinguishing similar functional groups on surfaces, then explore C-H activation by modifying adsorption configurations on surfaces. Finally, we discuss the bottom-up synthesis of atomically precise nanoribbons, which allows for the design of materials with tailored electronic properties.

2.2.1 Selective adsorption and activation of organic molecules on surfaces

For a highly symmetric molecule, selective adsorption on a surface can lead to selective activation, often driven by the lattice mismatch between the molecule and the surface [20]. For example, 4,4″-diamino-p-terphenyl (DATP), which has two identical amine end groups, exhibits distinct adsorption behaviors on Cu(111), named symmetric and dissymmetric adsorption. In the dissymmetric adsorption configuration (**Figure 2a**), two metastable adsorption sites exist: type IA (black) and type IB (red). Due to geometric mismatch, one amine group of type IA is above a FCC hollow site, while for type IB, one is above a top site and the other above an HCP hollow site. DFT calculations show type IA is ~8 meV more favorable than type IB, causing fluctuations between the two sites, separated by ~90 pm. In contrast, the symmetric configuration, with both amine groups bent toward the surface (**Figure 2b**), is less favorable than type I by 80–150 meV. The symmetric and dissymmetric configurations lead to different intermolecular behaviors. As shown in **Figure 2c**, 2-triphenylenecarbaldehyde (TPCA) molecules preferentially bind to the "fuzzy ends" of type I DATP, while connecting to both ends of symmetric type II DATP. This demonstrates selective activation of amine groups through selective adsorption on metal surfaces.

Similar to symmetry-breaking induced by selective adsorption at low energy levels, the selective C-H bond activation, typically occurring at high temperature, can also be achieved by the site-selective adsorption [5]. **Figure 2d** shows a nitrogen-containing polycyclic hydrocarbon (N-PH) molecule on an Ag(100) surface, featuring four quasi-equivalent C–H bonds labeled as α (blue) and β (red). In the C_2 symmetric precursor, the phonon energies of the C(sp3)-H stretching modes are nearly identical at the α and β sites, suggesting similar reactivity for C-H activation based on the oscillator approximation. However, when adsorbed on the C_{4h} symmetric Ag(100) substrate, the potential energy surface (PES) analysis in **Figure 2e** reveals that the most stable configuration occurs at a rotation angle of θ = 22°. In this configuration, the α-site carbon atom is positioned near a hollow site, while the β-site carbon is near an atop site of Ag(100). This results in different phonon energies of 355 meV and 361 meV for the C(sp3)-H stretching modes at the α and β sites, respectively. The lower vibrational frequency of the C(α)-H bond indicates it is more prone to dissociation compared to the C(β)-H bond, demonstrating selective C-H activation through site-selective adsorption. This is further supported by the calculated contribution of C(sp3)-H bonds to the highest occupied molecular orbital (HOMO) and the lowest unoccupied molecular orbital (LUMO), as shown in **Figure 2f** marked by stars. The term $RA_{C(\alpha)/C(\beta)}$, defined as the ratio of electron density in the HOMO contributed by C(α) to that from C(β), is consistently greater than 1. This indicates that the C(sp3) atoms at the α site are more reactive than those at the β site on the Ag(100) surface. By calculating the dehydrogenation energy barriers of the

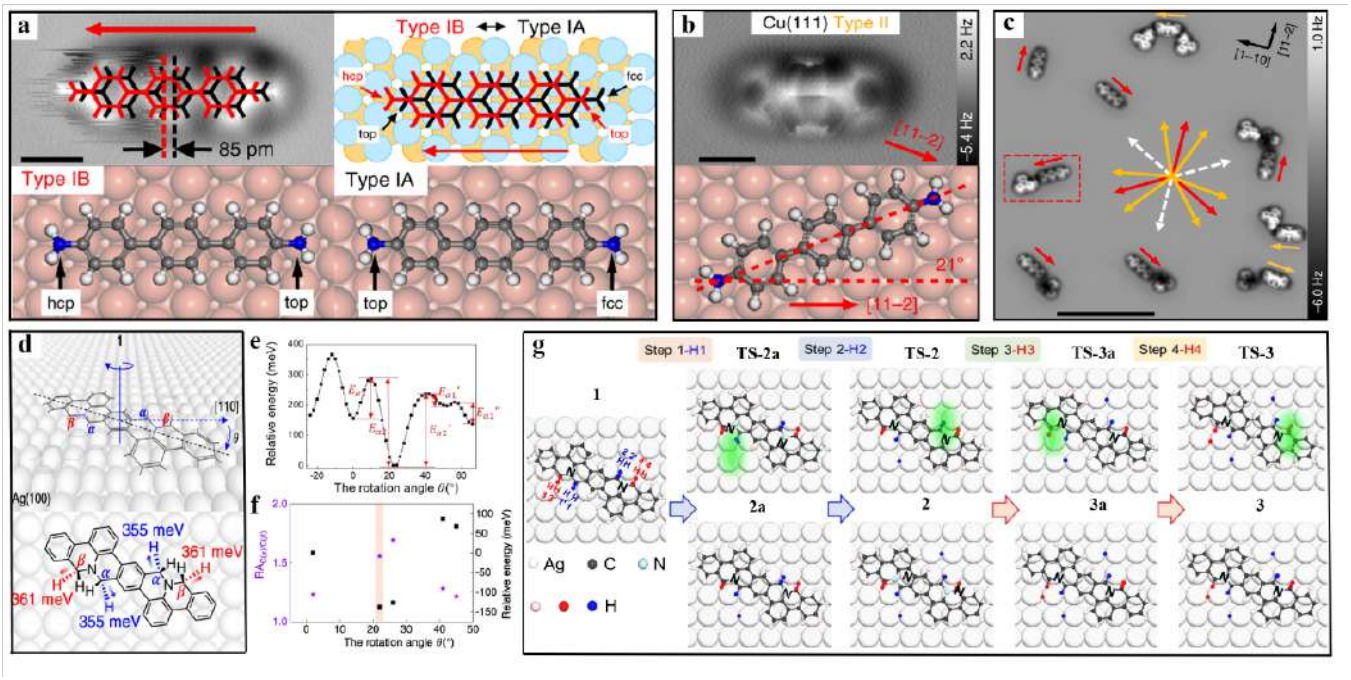

Figure 2. The structure, potential energy surface and relative reactivity of surface molecules adsorbed on the asymmetric active sites on the substrate. **a** Adsorption structure of DATP type I on Cu(111). **(Top left corner)** AFM image of DATP type I fitted by two molecular models, namely type IA (black) and type IB (red). **(Top right corner)** Sketch of precise adsorption positions as determined by atomic resolution AFM scans. The two structures are displaced by 96 pm along the [11−2] direction. **(Below)** DFT simulation of adsorption position type IA and type IB on Cu(111). Scale bar: 0.5 nm. **b** Adsorption structures of DATP type II on Cu(111). **(Top)** AFM image of DATP type II on Cu(111). **(Below)** DFT simulations of corresponding adsorption structures on Cu(111). Scale bar: 0.5 nm. **c** AFM image of self-assembly of DATP and TPCA molecules. Fuzzy sides of DATP type I molecules are indicated by red arrows. DATP type II structures are indicated by orange arrows. In total six orientations of DATP type II molecules exist, which are rotated by −21° and 21° with regard to the [11−2], [1−21], and [−211] directions. **d** Schematics of adsorption configuration of N-PH molecule on Ag(100) with different orientations. The long axis of molecule, the [110] direction of Ag(100), and rotation axis are marked with black dash line, blue dash arrow and blue line. The rotation angle is denoted by θ. **e** DFT calculated potential energy surface at different rotation angles θ. In each configuration, the molecule is fully relaxed in z direction. **f** The comparison of relative activity of C atoms at α and β sites ($RA_{C(\alpha)/C(\beta)}$, purple stars) and relative energy (black square) of each adsorption configuration with respect to the rotation angle θ. Relative energy is defined as the energy difference between different adsorption configurations and the one with a rotation angle of 2 degree. The most stable configuration with rotation angle $\theta = 22°$ is highlighted by a stripe in light coral. **g** The structure of initial state (1), transitional states (TS-2a, TS-2, TS-3a, TS-3), three metastable states (2a, 2, 3a) and final state (3) of dehydrogenation process used in the calculations. According to the energy profile, the dehydrogenation sequence is H1, H2, H3 and H4, which are highlighted by green ovals in the lower panel.

four C(sp3)-H bonds at α and β sites using the climbing image nudged elastic band (CI-NEB) method, it is proved that the dehydrogenation sequence is H1, H2, H3 and H4, which is in good agreement with the experimental results. **Figure 2g** presents the configurations of these intermediates.

2.2.2 Selective activation promoted bottom-up synthesis of graphene nanoribbons

Selective activation of organic molecules on surfaces provides an opportunity for atomically precise design of organic framework through bottom-up synthesis. Graphene nanoribbons (GNRs) have attracted intense interest due to their electronic, magnetic and topological properties, which provide next-generation materials for carbon-based nanoelectronics and spintronics [37]. Generally, in the bottom-up synthesis of graphene nanoribbons, selective activation involves two key effects, intermolecular C-C coupling and intramolecular cyclization. Intermolecular C-C coupling occurs through dehydrogenation of precursors and results in the formation of graphene nanoribbons with various shapes [7,38]. Intramolecular cyclization forms heterocyclic compounds and introduces significant doping effects [39]. Particularly, zigzag edge graphene nanoribbons (ZGNRs) are expected to host spin-polarized electronic edge states, and couple ferromagnetically along the edge and antiferromagnetically between the edges [40]. The bottom-up synthesis of ZGNRs via surface-assisted polymerization followed by cyclodehydrogenation represents a widely adopted methodology for fabricating atomically precise zigzag-edged nanostructures [41]. Notably, this approach affords the opportunity to incorporate heteroatom substitutions (e.g., sulfur, boron, and nitrogen) into the carbon framework, thereby enabling precise modulation of graphene nanoribbon electronic properties as demonstrated experimentally [42,43]. For example, NBN-doped zigzag-edge GNRs (NBN-ZGNR1 and NBN-ZGNR2) are achieved by the bottom-up synthesis [38]. **Figure 3a** presents a schematic diagram of the synthesis of ZGNRs via precursor polymerization on Au. Substituting C=C with B−N in the π-conjugated system can remarkably modulate the electronic structure. DFT results (**Figure 3b-g**) show that one-electron oxidation per NBN unit renders the band structure gapless and metallic (**Figure 3f, g**). Similar to ZGNRs, acenes (such as perylene, etc.) as a class of polycyclic aromatic hydrocarbons (PAHs)

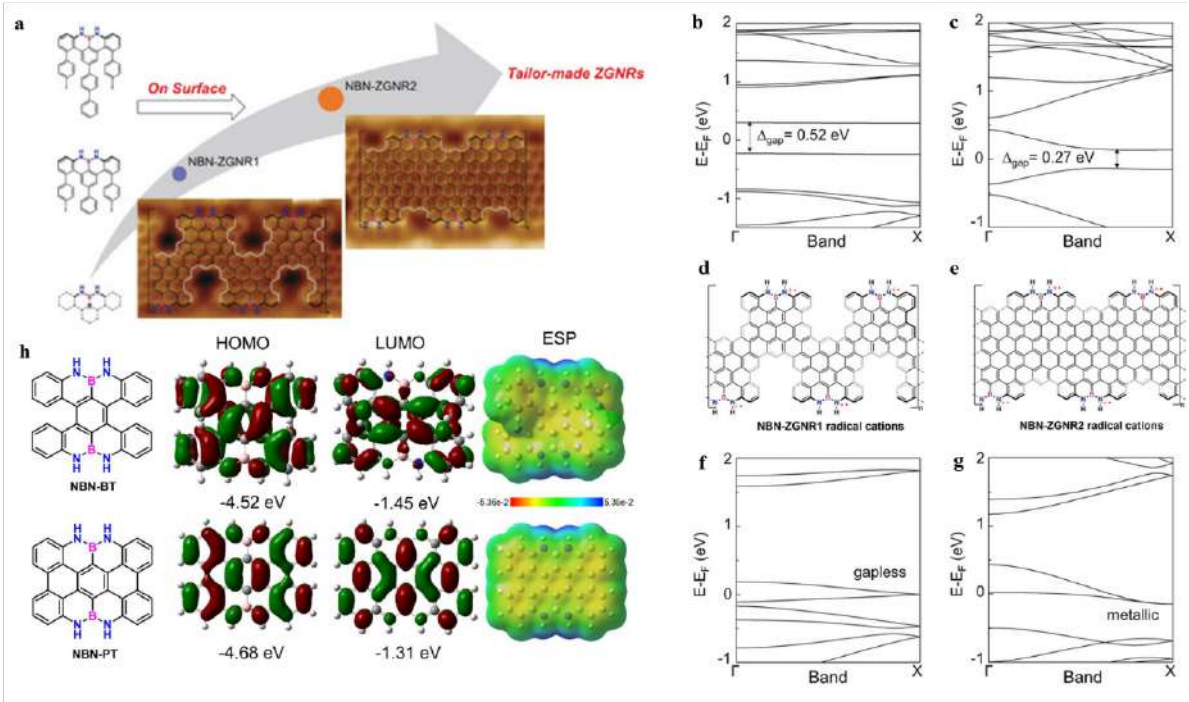

Figure 3. The synthetic pathways and the tunability of the electrical structure of graphene nanoribbons. **a** Schematic of NBN-doped ZGNRs synthesis and its STM images. **b**, **c** DFT-calculated band structures of pristine PCZGNR1 and PCZGNR2. **d**, **e** Chemical structures of NBN-ZGNR1 and NBN-ZGNR2 radical cations. **f**, **g** DFT-calculated band structures of NBN-ZGNR1 radical cations and NBN-ZGNR2 radical cations. **h** Calculated molecular orbitals, energy diagrams and Electrostatic Potential (ESP) maps of NBN-BT and NBN-PT. Positive (blue) signs indicate positive electron potential, and negative (red) signs indicate negative electron potential.

with zigzag edges, have attracted extensive attention in organic electronics and optoelectronics due to their unique electronic and physicochemical properties. However, they (such as peri-tetracene and above) suffer from poor stability at higher orders due to their open-shell multi-radical characteristics, which limits further research and application. Fu *et al.* introduced the first synthesis of NBN-doped bis-tetracene (NBN-BT) and peri-tetracene (NBN-PT) based on solution and surface-assisted synthesis [7]. By doping zigzag edges with B and N, the authors obtain stable higher-order acenes while tuning their electronic structures. **Figure 3h** shows the molecular orbital distribution and ESP maps of NBN-BT and NBN-PT calculated by DFT. Compared to all-carbon-based peri-tetracene (HOMO/LUMO/energy gap: −4.38/−2.62/1.76 eV), the different electronic properties and stabilities of NBN-BT and NBN-PT from bis-tetracene and peri-tetracene can be attributed to the unique NBN dopant units at the zigzag edges.

The NBN unit not only enhances the stability of NBN-BT but can also enables oxidation into the corresponding radical cation and dication, offering chemical tunability. NBN-BT undergoes two reversible oxidations. In the first step, NBN-BT form the NBN-BT monoradical cation ($[NBN\text{-}BT]^{+\cdot}$), which possesses an open-shell character. A possible product for the second oxidation step can be the NBN-BT diradical dication ($[NBN\text{-}BT]^{2+\cdot\cdot}$) or NBN-BT dication ($[NBN\text{-}BT]^{2+}$), which can be regarded as the isoelectronic structures of all-carbon-based bis-tetracene. Furthermore, through controlled continuous single-electron chemical or electrochemical oxidation, NBN-BT can be converted into its corresponding radical cation (0.88 eV) and further to dication (1.24 eV), which demonstrates a similar energy gap to its isoelectronic structure bis-tetracene (1.56 eV).

3. Interface-induced physical and chemical properties

In recent years, ferromagnetism and ferroelectricity, once believed to be absent in the two-dimensional limit, have been experimentally realized. The discovery of 2D ferromagnetism in Fe_3GeTe_2/Fe_3GaTe_2 [44,45] and VSe_2 [46], along with 2D ferroelectricity in SnTe [47], In_2Se_3 [48], $CuInP_2S_6$ [49] and $MoTe_2$ [50], as well as theoretical predictions of various 2D ferromagnetic and ferroelectric materials [51,52], underscores their unique low-dimensional properties. The rapid development of 2D materials has provided new opportunities for tailoring the physical and chemical properties through interface engineering. Their weak interlayer vdWs interactions allow precise control over interfacial configurations and electronic structures. Additionally, intercalating atoms or molecules at the interface can effectively tune interlayer interactions from weak vdWs forces to strong ionic or covalent bonds, leading to novel properties in these heterostructures.

3.1 Van der Waals stacking for tuning the multiferroic heterostructures

Ferroelectricity and ferromagnetism typically originate from different transition metal elements, making it challenging to achieve multiferroicity in conventional ferromagnetic materials. Constructing a 2D ferroelectric (FE) layer with a 2D ferromagnetic (FM) layer offers a promising approach to tuning multiferroic interactions at interfaces. For example, Jin *et al.* proposed a new method to control skyrmions and other complex spin textures by electric field utilizing the Dzyaloshinskii-Moriya interaction (DMI) [53]. A sandwich-like heterostructure, which is composed by two FE layers In_2Se_3 at the top and the bottom with a FM layer MnSeTe in the middle, has multiple states of magnetic skyrmions. **Figure 4a**

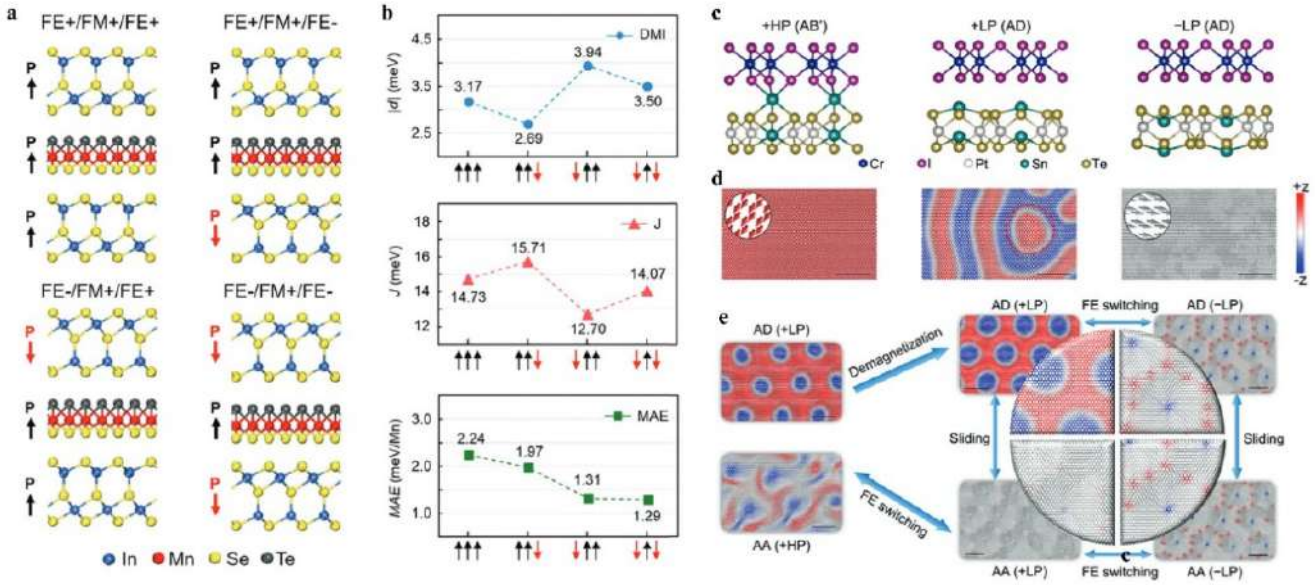

Figure 4. The modulation of magnetic parameters and the geometric and magnetic configurations of van der Waals heterojunctions. **a** Four possible configurations of the In_2Se_3/MnSeTe/In_2Se_3 heterostructure. **b** The absolute values of the DMI parameter (|d|), the exchange parameter J, and MAE of the heterostructure. **c** Three possible configurations at +HP, +LP, and −LP states. **d** Magnetic configurations for the three heterojunctions in **c** based on Monte Carlo simulations. **e** Reversible evolution of the magnetic configuration in the CrI_3/$Pt_2Sn_2Te_6$ heterojunction due to interlayer sliding and FE switching. The regular skyrmion lattice remains after demagnetization. The black scale bar corresponds to 10 nm.

shows the four possible polarization configurations considering the dipole directions within the top and the bottom FE layers. Compared to the results in **Figure 4b**, it is evident that the variation trend of the DMI coefficient in MnSeTe is always opposite to that of the exchange interaction coefficient in the process of polarization reversal. It indicates that by reversing the polarization of In_2Se_3, the magnetic parameters in MnSeTe can be significantly adjusted, thereby enabling multi-state control of magnetic skyrmions.

Instead of a sandwich structure with the FE top and bottom layers, a single 2D FE layer with quadruple-well potential itself is sufficient to induce various magnetic phases including Bloch-type skyrmions and novel magnetic superstructures [26]. **Figure 4c** presents the structure of the CrI_3/$Pt_2Sn_2Te_6$ heterostructure under different ferroelectric polarization states (+HP, +LP, and −LP) and stacking configurations (AB' and AD). The magnetic behavior of the FM layer (CrI_3) can be significantly influenced by changes in the ferroelectric polarization state of the FE layer ($Pt_2Sn_2Te_6$). Monte Carlo simulations reveal that the FM layer exhibits different magnetic alignment directions under various polarization states (as shown in **Figure 4d**). In the +LP (AD) state, spontaneous formation of Bloch-type skyrmions occurs in the FM layer (indicated by the red circle in **Figure 4d**). Further analysis demonstrates that the DMI-associated spin-orbit coupling energy is primarily contributed by the nonmagnetic iodine atoms in of CrI_3, which is consistent with the Fert-Levy mechanism. Notably, **Figure 4e** shows that in the +LP state with AD stacking, a regular skyrmion lattice can be stabilized by low-energy excitation. These skyrmions remain stable even after the removal of the external magnetic field, indicating nonvolatile control of magnetism.

Additionally, the interface also plays a vital role in breaking the forced symmetry to achieve the regulation of valley degrees of freedom. Zhu *et al.* summarized the laws for realizing anomalous valley Hall effect in hexagonal lattices and found that in the system, the antiferromagnetic order of the double layers can break the mirror symmetry of the space group, such as $TcGeSe_3$ with a space group of P_{-31m}, which is a necessary condition for realizing AVHE [54]. This way of using the interface to break symmetry can be generalized. In the absence of spontaneous ferroelectric-valley coupling, stacking is an effective method to change the symmetry of two-dimensional materials to induce ferroelectric-valley coupling.

3.2 Strong interaction stacking for functional heterostructures

Compared to the FE/FM interactions in vdWs stacking heterostructures, interlayer interactions in FE/FE bilayers are significantly stronger. It provides opportunities for intercalating metal atom into the vdWs gap and breaking the inversion symmetry, thus introducing strong spin−orbit coupling and tuning the magnetic properties. A strategy is proposed to eliminate Skyrmion Hall Effect (SkHE) by intercalating nonmagnetic elements into van der Waals bilayer ferromagnets featuring in-plane ferromagnetism [55], in which the relatively heavy nonmagnetic atoms is crucial for DMI generation. Utilizing high throughput calculations, SrV_2Se_4 and BaV_2Se_4, which are composed with the bilayer 1T-VSe_2 and the intercalated Sr/Ba atoms, have achieved for robust high-speed Skyrmion racetrack memory devices. **Figure 5a** and **5b** shows the intercalation structures of SrV_2Se_4 and BaV_2Se_4, which have central-inversional and mirror symmetry, respectively. Monte Carlo (MC) simulations are performed to determine low-energy spin textures, as shown in **Figure 5c−f.** According to the symmetry and the topological characteristics, 10 spin textures are obtained (**Figure 5g**). The topologically protected spin textures remain stable under finite external magnetic fields, making it promising candidate in spintronics.

Following the FAIR principles, several major databases have been developed to support the Materials Genome Project. SpringerMaterials and the Materials Project provide comprehensive data on over 500,000 materials, including crystal and band structures,

density, and thermodynamics [56]. For example, Winther *et al*. created a surface catalysis database with over 100,000 entries focused on bimetallic alloys [57]. Borysov *et al*. developed an organic materials database centered on electronic structures [58]. Liang *et al*. built the Atomly database, covering 300,000+ inorganic crystals, with notable progress in qubit and 2D materials [59]. Du *et al.* constructed 2D material interface and charged building block databases using multi-scale simulations [60,61]. Except for the covalent bond formed by the intercalated metal atom, the heterostructures by stacking 2D layers with positive and negative charges are achieved as functional-oriented materials [61]. Using a topological-scaling algorithm, as shown in **Figure 5h,** 1028

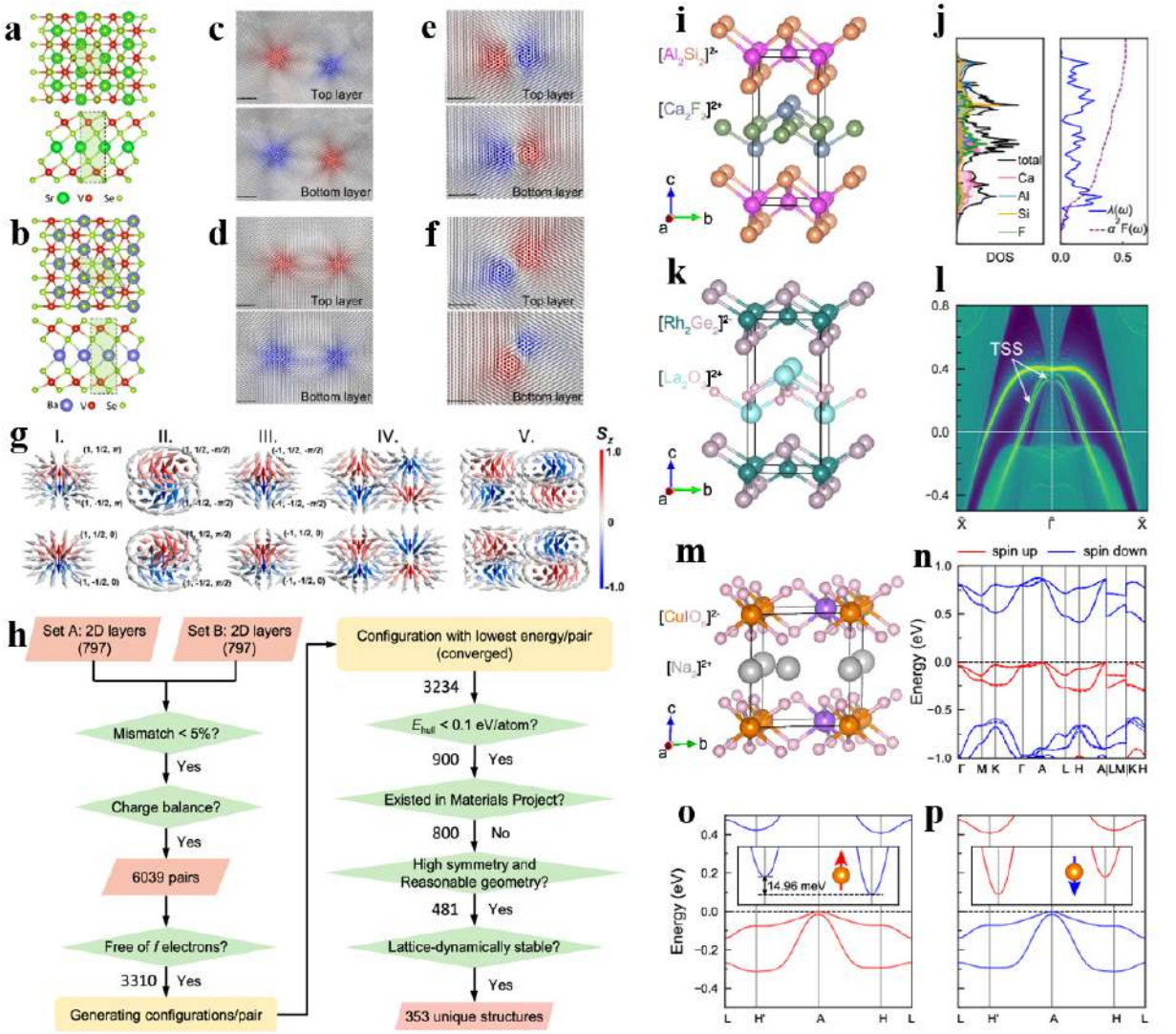

Figure 5. The configurations of interface-layered strong-interaction heterostructures and the construction of an ionic layered material database. (**a**-**g**) Structures and topological spin textures of MV_2Se_4 monolayers (M = Sr, Ba). **a** and **b** Top and side views of SrV_2Se_4 and BaV_2Se_4, respectively. The light green area indicates a unit cell. (**c**-**f**) Monte Carlo simulations of magnetic configurations of MV_2Se_4 without external field. **c** and **e** The zoom-in spin textures of SrV_2Se_4 on interlayer bimeron and interlayer quadmeron, respectively. **d** and **f** The zoom-in spin textures of BaV_2Se_4 on interlayer bimeron and interlayer quadmeron, respectively. The gray spins represent in-plane ferromagnetic backgrounds, while colors are assigned for the positive (red) or negative (blue) out-of-plane components of spins. **g** Five types of spin texture forms with *SrDQ* in MV_2Se_4, as can be distinguished by (m, p, γ). The black line segment inserted in all panels indicates a scale bar of 5 nm. **h** Workflow for construction of layered materials by stacking 2D charged building blocks. Only 797 2D charged building blocks with tetragonal, trigonal, and hexagonal symmetry and number of atoms less than 10 are considered as input to construct layered structures. The numbers on the left side of each procedure show the remaining ones after a specific procedure. (**i**-**l**) Superconductivity of CaAlSiF and band topology of LaRhGeO. **i** Crystal structure of CaAlSiF. **j** Phonon density of states (left) and Eliashberg function $\alpha^2F(\omega)$ as well as the electron–phonon coupling strength $\lambda(\omega)$ (right) for CaAlSiF. **k** Crystal structure of LaRhGeO. **l** Topological surface state (TSS) of (010) plane for LaRhGeO. The color in the electronic structure indicates the states contributed by distinct elements/orbitals, and that in the phonon dispersion shows the strength of electron–phonon coupling λ_{qv}. (**m**-**p**) Bipolar ferromagnetic semiconducting and anomalous valley Hall effect of Na_2CuIO_6. **m** Crystal structure of Na_2CuIO_6. **n** Electronic structure without SOC (dashed line) and with SOC (solid line). valley-splitting with Cu spins aligning **o** +z direction and **p** −z direction.

charged 2D building blocks (BBs) were identified, showcasing versatile functionalities like superconductivity, magnetism, and topological properties. By assembling these BBs with valence state and lattice mismatch considerations, 353 stable layered materials were predicted via high-throughput calculations with novel properties compared with their parent materials. In the ionic layered structure, the anionic layer and the cationic layer are interlaced, performing as functions and charge reservoirs, respectively. Therefore, the ionic layers can be broadly classified into functional layers and carrier layers [62]. Specifically, tuning the charge state of the cationic layer can modulate the functional layer into a hole- or electron-doped state, giving rise to novel properties. For example, modulating the charge reservoirs in LnPdAsO (Ln = La, Ce, Pr) induces a negatively charged Pd state, where enhanced electron accumulation on Pd directly reduces the hydrogen evolution reaction overpotential and improves catalytic efficiency [63]. As shown in **Figure 5(i-p)**, CaAlSiF displays superconducting transition temperature higher than NaAlSi; Na_2CuIO_6 shows bipolar ferromagnetic semiconductivity and anomalous valley Hall effect that are absent in $KCuIO_6$; LaRhGeO possesses nontrivial band topology. The interlayer charge transfer not only enables this tunability but also contributes to the structural stability and cohesion.

4. Conclusion and outlook

The study of physical and chemical phenomena at surfaces and interfaces has a long history. Recent developments in data-driven high-throughput and machine learning technologies have accelerated the discovery of new materials and unveiled novel physical and chemical insights. In this review, we highlight several chemical and physical properties at surfaces and interfaces, and the construction of databases based on a deep understanding of surface/interface interactions.

For the further developments in computational surface/interface science, it is crucial to improve exchange-correlation functionals and van der Waals corrections in order to achieve higher computational accuracy. Furthermore, the coupling effects of electric and magnetic fields at finite temperatures must be quantitatively addressed to resolve experimental challenges. Continued development of computational technologies, particularly through the development of advanced machine learning models, will be pivotal in driving further innovations in this field.

Acknowledgements

We acknowledge the financial support from the National Natural Science Foundation of China (62488201, 52272172), the National Key Research and Development Program of China (2022YFA1204100), the Major Program of National Natural Science Foundation of China (92163206). Computational resources were provided by the National Supercomputing Center in Tianjin.

References

[1] Wan, K., He, J., Shi, X. Construction of high accuracy machine learning interatomic potential for surface/interface of nanomaterials—a review. *Adv Mater*, **36** (2024), 2305758.

[2] Tao, L., Zhang, Y.-Y., Du, S. Structures and electronic properties of functional molecules on metal substrates: From single molecule to self-assemblies. *WIREs Computational Molecular Science*, **12** (2022), e1591.

[3] Du, S. X., Gao, H. J., Seidel, C., Tsetseris, L., Ji, W., Kopf, H., Chi, L. F., Fuchs, H., Pennycook, S. J., Pantelides, S. T. Selective nontemplated adsorption of organic molecules on nanofacets and the role of bonding patterns. *Phys Rev Lett*, **97** (2006), 156105.

[4] Ren, J., Freitag, M., Gao, Y., Bellotti, P., Das, M., Schulze Lammers, B., Mönig, H., Zhang, Y., Daniliuc, C. G., Du, S. Reversible self-assembly of an N-heterocyclic carbene on metal surfaces. *Angewandte Chemie International Edition*, **61** (2022), e202115104.

[5] Gao, Y., Huang, L., Cao, Y., Richter, M., Qi, J., Zheng, Q., Yang, H., Ma, J., Chang, X., Fu, X. Selective activation of four quasi-equivalent C–H bonds yields N-doped graphene nanoribbons with partial corannulene motifs. *Nat Commun*, **13** (2022), 6146.

[6] Yang, K., Chen, H., Pope, T., Hu, Y., Liu, L., Wang, D., Tao, L., Xiao, W., Fei, X., Zhang, Y.-Y. Tunable giant magnetoresistance in a single-molecule junction. *Nat Commun*, **10** (2019), 3599.

[7] Fu, Y., Chang, X., Yang, H., Dmitrieva, E., Gao, Y., Ma, J., Huang, L., Liu, J., Lu, H., Cheng, Z. NBN-doped bis-tetracene and peri-tetracene: Synthesis and characterization. *Angewandte Chemie International Edition*, **60** (2021), 26115-26121.

[8] Yang, J., Pan, J., Zhang, Y.-F., Wan, G., Zhu, Y., Wei, Z., Li, Y., Du, S. 1D crystalline assemblies exhibiting large second harmonic generation susceptibilities and stacking-/polarization-driven tunability. *Adv Funct Mater*, **35** (2025), 2411889.

[9] Yang, J., Deng, J., Pan, J., Zhu, Y., Zhang, Y.-F., Li, Y., Sun, J.-T., Du, S. 1D van der Waals polymers with nonlinear optical performance approaching theoretical upper limit. *Adv Funct Mater*, **33** (2023), 2305731.

[10] Li, P., Gao, L., Tao, L., Pan, J., Lim, F. H., Zhang, Y.-F., Du, S. Semiconducting scandium/yttrium chalcohalides: Promising visible-light-driven photocatalysts for overall water splitting. *ACS Catalysis*, ** (2025), 4533-4540.

[11] Pan, J., Yu, J., Zhang, Y.-F., Du, S., Janotti, A., Liu, C.-X., Yan, Q. Quantum anomalous hall effect in two-dimensional magnetic insulator heterojunctions. *Npj Comput Mater*, **6** (2020), 152.

[12] Deng, J., Pan, J., Zhang, Y., Li, Y., Dong, W., Sun, J., Du, S. Screening and design of bipolar magnetic-semiconducting monolayers and heterostructures. *ACS Applied Electronic Materials*, **4** (2022), 3232-3239.

[13] Qi, J., Gao, Y., Jia, H., Richter, M., Huang, L., Cao, Y., Yang, H., Zheng, Q., Berger, R., Liu, J. Force-activated isomerization of a single molecule. *J Am Chem Soc*, **142** (2020), 10673-10680.

[14] Panasci, S. E., Schilirò, E., Roccaforte, F., Giannazzo, F. Gold-assisted exfoliation of large-area monolayer transition metal dichalcogenides: From interface properties to device applications. *Adv Funct Mater*, **35** (2025), 2414532.

[15] Feng, M., Gao, L., Deng, Z., Ji, W., Guo, X., Du, S., Shi, D., Zhang, D., Zhu, D., Gao, H. Reversible, erasable, and rewritable nanorecording on an H2 rotaxane thin film. *J Am Chem Soc*, **129** (2007), 2204-2205.

[16] Shang, Y., Wen, Y., Li, S., Du, S., He, X., Cai, L., Li, Y., Yang, L., Gao, H., Song, Y. A triphenylamine-containing donor−acceptor molecule for stable, reversible, ultrahigh density data storage. *J Am Chem Soc*, **129** (2007), 11674-11675.

[17] Jiang, G., Michinobu, T., Yuan, W., Feng, M., Wen, Y., Du, S., Gao, H., Jiang, L., Song, Y., Diederich, F. Crystalline thin film of a donor-substituted cyanoethynylethene for nanoscale data recording through intermolecular charge-transfer interactions. *Adv Mater*, **17** (2005), 2170-2173.

[18] Wu, H. M., Song, Y. L., Du, S. X., Liu, H. W., Gao, H. J., Jiang, L., Zhu, D. B. Nanoscale data recording on an organic monolayer film. *Adv Mater*, **15** (2003), 1925-1929.

[19] Feng, M., Guo, X., Lin, X., He, X., Ji, W., Du, S., Zhang, D., Zhu, D., Gao, H. Stable, reproducible nanorecording on rotaxane thin films. *J Am Chem Soc*, **127** (2005), 15338-15339.

[20] Zhong, Q., Ebeling, D., Tschakert, J., Gao, Y., Bao, D., Du, S., Li, C., Chi, L., Schirmeisen, A. Symmetry breakdown of 4,4″-diamino-p-terphenyl on a Cu(111) surface by lattice mismatch. *Nat Commun*, **9** (2018), 3277.

[21] Gao, L., Liu, Q., Zhang, Y. Y., Jiang, N., Zhang, H. G., Cheng, Z. H., Qiu, W. F., Du, S. X., Liu, Y. Q., Hofer, W. A. Constructing an array of anchored single-molecule rotors on gold surfaces. *Phys Rev Lett*, **101** (2008), 197209.

[22] Liu, Q., Zhang, Y. Y., Jiang, N., Zhang, H. G., Gao, L., Du, S. X., Gao, H. J. Identifying multiple configurations of complex molecules in dynamical processes: Time resolved tunneling spectroscopy and density functional theory calculation. *Phys Rev Lett*, **104** (2010), 166101.

[23] Chen, H., Pope, T., Wu, Z.-Y., Wang, D., Tao, L., Bao, D.-L., Xiao, W., Zhang, J.-L., Zhang, Y.-Y., Du, S. Evidence for ultralow-energy vibrations in large organic molecules. *Nano Lett*, **17** (2017), 4929-4933.

[24] Lu, H.-L., Cao, Y., Qi, J., Bakker, A., Strassert, C. A., Lin, X., Ernst, K.-H., Du, S., Fuchs, H., Gao, H.-J. Modification of the potential landscape of molecular rotors on Au(111) by the presence of an STM tip. *Nano Lett*, **18** (2018), 4704-4709.

[25] Li, Y., Deng, J., Zhang, Y.-F., Jin, X., Dong, W.-H., Sun, J.-T., Pan, J., Du, S. Nonvolatile electrical control of spin polarization in the 2D bipolar magnetic semiconductor VSeF. *Npj Comput Mater*, **9** (2023), 50.

[26] Li, P., Tao, L., Jin, X., Wan, G., Zhang, J., Zhang, Y.-F., Sun, J.-T., Pan, J., Du, S. Nonvolatile multistate manipulation of topological magnetism in monolayer CrI3 through quadruple-well ferroelectric materials. *Nano Lett*, **24** (2024), 2345-2351.

[27] Urbani, M., Ragoussi, M.-E., Nazeeruddin, M. K., Torres, T. Phthalocyanines for dye-sensitized solar cells. *Coordination Chemistry Reviews*, **381** (2019), 1-64.

[28] Tao, L., Guo, W., Zhang, Y.-Y., Zhang, Y.-F., Sun, J., Du, S., Pantelides, S. T. Quantum nutcracker for near-room-temperature H2 dissociation. *Science Bulletin*, **64** (2019), 4-7.

[29] Wu, S. W., Nazin, G. V., Chen, X., Qiu, X. H., Ho, W. Control of relative tunneling rates in single molecule bipolar electron transport. *Phys Rev Lett*, **93** (2004), 236802.

[30] Ji, W., Lu, Z.-Y., Gao, H. Electron core-hole interaction and its induced ionic structural relaxation in molecular systems under X-ray irradiation. *Phys Rev Lett*, **97** (2006), 246101.

[31] Gao, L., Ji, W., Hu, Y. B., Cheng, Z. H., Deng, Z. T., Liu, Q., Jiang, N., Lin, X., Guo, W., Du, S. X. Site-specific Kondo effect at ambient temperatures in iron-based molecules. *Phys Rev Lett*, **99** (2007), 106402.

[32] Chen, H., Tao, L., Wang, D., Wu, Z.-Y., Zhang, J.-L., Gao, S., Xiao, W., Du, S., Ernst, K.-H., Gao, H.-J. Stereoselective on-surface cyclodehydrofluorization of a tetraphenylporphyrin and homochiral self-assembly. *Angewandte Chemie International Edition*, **59** (2020), 17413-17416.

[33] Yixuan, G., Lei, T., Dongfei, W., Hui, G., Hui, C. Tuning the magnetic coupling of a porphyrin with the substrate through the intramolecular cyclization reaction. *Chin. Phys. Lett.*, **42** (2025), 037402.

[34] Gao, Y., Tao, L., Wang, D., Guo, H., Chen, H. Two-dimensional Kondo array of phthalocyanine-porphyrin bimolecular self-assembled systems. *Phys Rev B*, **111** (2025), 035408.

[35] Gao, Y., Zhang, Y.-Y., Sun, J.-T., Zhang, L., Zhang, S., Du, S. Quantum anomalous Hall effect in two-dimensional Cu-dicyanobenzene coloring-triangle lattice. *Nano Research*, **13** (2020), 1571-1575.

[36] Gao, Y., Tao, L., Yin, Y., Wang, H., Ge, Y. Tailoring electrocatalytic hydrogen evolution activity in topological triangular metal–organic frameworks. *Advanced Sustainable Systems*, **n/a**, 2400622.

[37] Han, W., Kawakami, R. K., Gmitra, M., Fabian, J. Graphene spintronics. *Nat Nanotechnol*, **9** (2014), 794-807.

[38] Fu, Y., Yang, H., Gao, Y., Huang, L., Berger, R., Liu, J., Lu, H., Cheng, Z., Du, S., Gao, H.-J. On-surface synthesis of NBN-doped zigzag-edged graphene nanoribbons. *Angewandte Chemie International Edition*, **59** (2020), 8873-8879.

[39] Kawai, S., Saito, S., Osumi, S., Yamaguchi, S., Foster, A. S., Spijker, P., Meyer, E. Atomically controlled substitutional boron-doping of graphene nanoribbons. *Nature Communications*, **6** (2015), 8098.

[40] Nakada, K., Fujita, M., Dresselhaus, G., Dresselhaus, M. S. Edge state in graphene ribbons: Nanometer size effect and edge shape dependence. *Phys Rev B*, **54** (1996), 17954-17961.

[41] Ruffieux, P., Wang, S., Yang, B., Sánchez-Sánchez, C., Liu, J., Dienel, T., Talirz, L., Shinde, P., Pignedoli, C. A., Passerone, D. On-surface synthesis of graphene nanoribbons with zigzag edge topology. *Nature*, **531** (2016), 489-492.

[42] Cai, J., Pignedoli, C. A., Talirz, L., Ruffieux, P., Söde, H., Liang, L., Meunier, V., Berger, R., Li, R., Feng, X. Graphene nanoribbon heterojunctions. *Nat Nanotechnol*, **9** (2014), 896-900.

[43] Cloke, R. R., Marangoni, T., Nguyen, G. D., Joshi, T., Rizzo, D. J., Bronner, C., Cao, T., Louie, S. G., Crommie, M. F., Fischer, F. R. Site-specific substitutional boron doping of semiconducting armchair graphene nanoribbons. *J Am Chem Soc*, **137** (2015), 8872-8875.

[44] Deiseroth, H.-J., Aleksandrov, K., Reiner, C., Kienle, L., Kremer, R. K. Fe3GeTe2 and Ni3GeTe2 – two new layered transition-metal compounds: Crystal structures, hrtem investigations, and magnetic and electrical properties. *European Journal of Inorganic Chemistry*, **2006** (2006), 1561-1567.

[45] Zhang, G., Guo, F., Wu, H., Wen, X., Yang, L., Jin, W., Zhang, W., Chang, H. Above-room-temperature strong intrinsic ferromagnetism in 2D van der Waals Fe3GaTe2 with large perpendicular magnetic anisotropy. *Nat Commun*, **13** (2022), 5067.

[46] Xu, K., Chen, P., Li, X., Wu, C., Guo, Y., Zhao, J., Wu, X., Xie, Y. Ultrathin nanosheets of vanadium diselenide: A metallic two-dimensional material with ferromagnetic charge-density-wave behavior. *Angewandte Chemie International Edition*, **52** (2013), 10477-10481.

[47] Chang, K., Liu, J., Lin, H., Wang, N., Zhao, K., Zhang, A., Jin, F., Zhong, Y., Hu, X., Duan, W. Discovery of robust in-plane ferroelectricity in atomic-thick SnTe. *Science*, **353** (2016), 274-278.

[48] Ding, W., Zhu, J., Wang, Z., Gao, Y., Xiao, D., Gu, Y., Zhang, Z., Zhu, W. Prediction of intrinsic two-dimensional ferroelectrics in In2Se3 and other III2-VI3 van der Waals materials. *Nat Commun*, **8** (2017), 14956.

[49] Brehm, J. A., Neumayer, S. M., Tao, L., O'Hara, A., Chyasnavichus, M., Susner, M. A., McGuire, M. A., Kalinin, S. V., Jesse, S., Ganesh, P. Tunable quadruple-well ferroelectric van der Waals crystals. *Nat Mater*, **19** (2020), 43-48.

[50] Yuan, S., Luo, X., Chan, H. L., Xiao, C., Dai, Y., Xie, M., Hao, J. Room-temperature ferroelectricity in MoTe2 down to the atomic monolayer limit. *Nat Commun*, **10** (2019), 1775.

[51] Jin, X., Tao, L., Zhang, Y.-Y., Pan, J., Du, S. Intrinsically scale-free ferroelectricity in two-dimensional M2X2Y6. *Nano Research*, **15** (2022), 3704-3710.

[52] Liu, Z., Tao, L., Zhang, Y.-Y., Pan, J., Du, S. Designing two-dimensional ferroelectric materials from phosphorus-analogue structures. *Nano Research*, **16** (2023), 5834-5842.

[53] Jin, X., O'Hara, A., Zhang, Y.-Y., Du, S., Pantelides, S. T. Designing strong and tunable magnetoelectric coupling in 2D trilayer heterostructures. *2D Materials*, **10** (2023), 015007.

[54] Zhu, Y., Sun, J.-T., Pan, J., Deng, J., Du, S. Enforced symmetry breaking for anomalous valley hall effect in two-dimensional hexagonal lattices. *Phys Rev Lett*, **134** (2025), 046403.

[55] Zhang, X., Wan, G., Zhang, J., Zhang, Y.-F., Pan, J., Du, S. Eliminating skyrmion hall effect in ferromagnetic skyrmions. *Nano Lett*, **24** (2024), 10796-10804.

[56] Jain, A., Ong, S. P., Hautier, G., Chen, W., Richards, W. D., Dacek, S., Cholia, S., Gunter, D., Skinner, D., Ceder, G. Commentary: The materials project: A materials genome approach to accelerating materials innovation. *APL Materials*, **1** (2013).

[57] Winther, K. T., Hoffmann, M. J., Boes, J. R., Mamun, O., Bajdich, M., Bligaard, T.

[58] Borysov, S. S., Geilhufe, R. M., Balatsky, A. V., Organic materials database: An open-access online database for data mining, *PLOS ONE*, 12 (2017) e0171501.

[59] Liang, Y., Chen, M., Wang, Y., Jia, H., Lu, T., Xie, F., Cai, G., Wang, Z., Meng, S., Liu, M. A universal model for accurately predicting the formation energy of inorganic compounds, *Science China Materials*, 66 (2023) 343-351.

[60] Xian-Li, Z., Jinbo, P., Xin, Yan-Fang, Z., Jia-Tao, S., Yu-Yang, Z., Shixuan, D. Database construction for two-dimensional material-substrate interfaces, *Chin. Phys. Lett*., 38 (2021) 066801-066801.

[61] Deng, J., Pan, J., Zhang, Y.-F., Du, S. Database construction of two-dimensional charged building blocks for functional-oriented material design, *Nano Lett*, 23 (2023) 4634-4641.

[62] Kabbour, H., Cario, L., Boucher, F. Rational design of new inorganic compounds with the ZrSiCuAs structure type using 2D building blocks, *Journal of Materials Chemistry*, 15 (2005) 3525-3531.

[63] Chen, X., Guo, J., Deng, J., Wang, R., Zhao, S., Chen, N., Gou, H., Song, B., Chen, X. Highly active sites in quaternary LnPdAsO (Ln = La, Ce, Pr) with excellent catalytic activity for hydrogen evolution reaction, *ACS Applied Energy Materials*, 4 (2021) 4302-4307.